NANO LETTERS

pubs.acs.org/NanoLett

Letter

Growth and Self-Assembly of $CsPbBr_3$ Nanocrystals in the TOPO/$PbBr_2$ Synthesis as Seen with X-ray Scattering

Federico Montanarella,* Quinten A. Akkerman, Dennis Bonatz, Maaike M. van der Sluijs, Johanna C. van der Bok, P. Tim Prins, Marcel Aebli, Alf Mews, Daniel Vanmaekelbergh, and Maksym V. Kovalenko*

Cite This: *Nano Lett.* 2023, 23, 667–676

Read Online

ACCESS | Metrics & More | Article Recommendations | Supporting Information

ABSTRACT: Despite broad interest in colloidal lead halide perovskite nanocrystals (LHP NCs), their intrinsic fast growth has prevented controlled synthesis of small, monodisperse crystals and insights into the reaction mechanism. Recently, a much slower synthesis of LHP NCs with extreme size control has been reported, based on diluted TOPO/$PbBr_2$ precursors and a diisooctylphosphinate capping ligand. We report new insights into the nucleation, growth, and self-assembly in this reaction, obtained by *in situ* synchrotron-based small-angle X-ray scattering and optical absorption spectroscopy. We show that dispersed 3 nm $Cs[PbBr_3]$ agglomerates are the key intermediate species: first, they slowly nucleate into crystals, and then they release $Cs[PbBr_3]$ monomers for further growth of the crystals. We show the merits of a low $Cs[PbBr_3]$ monomer concentration for the reaction based on oleate ligands. We also examine the spontaneous superlattice formation mechanism occurring when the growing nanocrystals in the solvent reach a critical size of 11.6 nm.

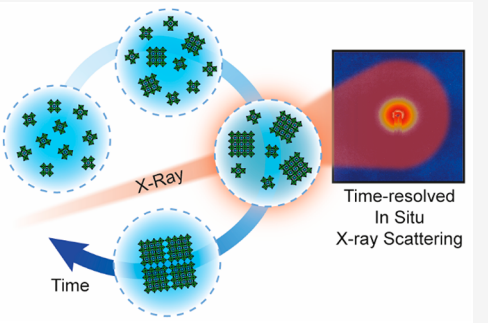

KEYWORDS: *lead halides, perovskites, nanocrystals, growth, in situ, quantum dots, self-assembly, X-ray scattering*

Ligand-capped colloidal nanocrystals (NCs) of lead halide perovskite (LHP), especially cesium lead halide ($CsPbX_3$; X = Cl, Br, I), are the latest generation of visible-light-emissive semiconductor NCs. So far, they have been produced via facile and fast ionic coprecipitation. They exhibit near-unity photoluminescence efficiency, even without surface shelling for electronic passivation, and high defect tolerance.[1−6] These NCs have attracted attention as single-photon emitters[7−10] and also feature aggregated emissive states.[11−15] LHP NCs are actively pursued for diverse applications, foremost in light-emitting diodes[16−18] and downconversion displays,[19−21] as well as scintillators,[22−24] photodetectors,[22,25−29] printed security tags,[30,31] etc. Despite their accelerated practical deployment, the literature on the synthesis of LHP NCs continues to expand; the variants of diverse synthesis protocols keep increasing, differing in, for instance, the precursors, ligand chemistry, solvents, NC surface treatments, and other postsynthetic processing steps.[32−44] By and large, the motivation behind these intense synthesis efforts is rooted in the challenges that arise from the inherently soft and labile nature of these ionic semiconductors.

From early on, the inherently fast kinetics of the ionic coprecipitation reactions was the major hurdle for size control, especially in the small-size regime of strong quantum confinement. Specifically, the common reactions, such as the standard oleic acid−oleylamine hot-injection synthesis (OA/OlAm),[1] are nearly instantaneous, since relevant cationic (Cs^+) and anionic ($PbBr_3^-$) species are present from the beginning. Typical protocols that rely on mixing liquids in practically relevant quantities (milliliter to liter) are therefore characterized by very fast nucleation and growth rates. In these cases, state-of-the-art *in situ* optical absorption spectroscopy and X-ray scattering methods, capable of handling millisecond time scales,[45,46] still yield unsatisfactory outcomes. The challenge of resolving the early formation stage of perovskite NCs was not even fully mitigated when the same OA/OlAm synthesis was conducted in nanoliter-sized droplets using microfluidic platforms that assured mixing-to-homogenization times of under 300 ms and a mixing-to-optical-spectrum-acquisition time under 100 ms.[47,48] Self-evidently, synthesis methods relying on very fast reactions lack the option of isolating a desired NC size fraction by controlling the growth time, a common convenient practice for other semiconductor NCs.[49,50]

We recently introduced a room-temperature synthesis of $CsPbBr_3$ NCs with growth times of up to 30 min.[51] Such a

Received: November 17, 2022
Revised: December 29, 2022
Published: January 6, 2023

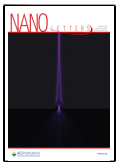

https://doi.org/10.1021/acs.nanolett.2c04532
Nano Lett. 2023, 23, 667−676

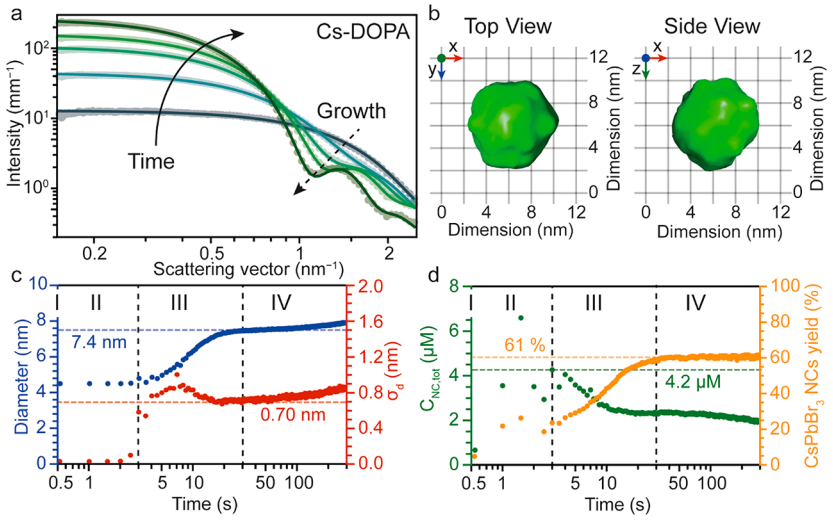

Figure 1. *In situ* time-resolved synchrotron-based SAXS results of the TOPO/$PbBr_2$ synthesis. (a) Five representative SAXS patterns (data points) with their corresponding fits (solid lines) collected during the formation of $CsPbBr_3$ NCs at 0.5, 5.5, 10.5, 15.5, and 300 s, respectively. The formation of NCs uniform in size manifests itself as local minima at higher values of scattering vector **q**. (b) Average particle model obtained by independently fitting the last scattering curve (t = 300 s) with a shape-retrieval, dummy-atom-model based algorithm.[62] The particles are characterized by a quasi-spherical (rhombicuboctahedral) shape and a size of ~8.1 nm. (c) Average size of the nanocrystals (blue) and standard deviation (red) as a function of the reaction time. The Roman numbers indicate the different phases of the synthesis. (d) NC concentration (green) and $CsPbBr_3$ yield (orange; calculated on the yield of the deficient species, i.e. Cs) as a function of the reaction time. The two dotted vertical lines separate the different phases of the NC formation. The Roman numbers indicate the different phases of the synthesis.

drastic reduction in the reaction rates primarily arises from the intricate solution equilibria involving the precursors ($PbBr_2$ coordinated by trioctylphosphine oxide (TOPO) and Cs-DOPA (DOPA = diisooctylphosphinate)), the monomer intermediates, i.e., Cs[$PbBr_3$] species coordinated by TOPO (see below), and the resulting $CsPbBr_3$ NCs and other formed Pb species ($Pb(DOPA)_2$). Importantly, in the absence of amines and acids in the Pb precursor solution, the addition of Cs-DOPA specifically causes the formation of the equivalent quantity of bromoplumbate ($PbBr_3^-$) and Cs[$PbBr_3$] species. The new method resulted in an unprecedented resolution of excitonic features (with up to three higher excitonic transitions) across a broad range of NC sizes (3−14 nm), stemming from both narrow size dispersion and nearly spherical (i.e. rhombicuboctahedral) shapes.[51,52] *In situ* absorption spectroscopy was highly instrumental for tracing the evolution of NCs and depletion of precursors, enabling us to study equilibria essential for the NC formation kinetics. To fulfill the technical requirements of the *in situ* absorption spectroscopy (optical densities matching the dynamic range of detectors), the TOPO/$PbBr_2$ synthesis was optimized to yield $CsPbBr_3$ NC concentrations substantially lower than those typically used for perovskite and other semiconductor NCs (molarity of deficient species: ca. (0.1−0.5) × 10^{-3} M versus ca. (7−12) × 10^{-3} M,[1,53] and ca. (5−10) × 10^{-2} M.[54,55]). We also note that absorption spectroscopy alone might not be sufficient to obtain direct information on the size and morphology of dispersed particles, on the nucleating and growing NCs or on their uniformity and temporal evolution during the synthesis. These tasks are uniquely matched by (*in situ*) small-angle and wide-angle X-ray scattering methods (SAXS and WAXS, respectively), especially using synchrotron-based X-rays with unmatched brilliance. Such experiments have proven indispensable for studying colloidal NCs.[45,46,56−61]

In this work, we monitored the entire lifespan of $CsPbBr_3$ NCs in the TOPO/$PbBr_2$ synthesis—from their nucleation to self-assembly into superlattices in the same reaction vessel—using synchrotron-based SAXS and *in situ* absorption spectroscopy. The synthesis was adjusted to ca. 30-fold higher concentrations (concentration of deficient species ca. (4−7) × 10^{-3} M) compared to those in ref 51, in line with common synthesis conditions for perovskite NCs[1] but retaining sufficiently slow overall kinetics for a complete characterization. We followed the formation of the NCs, proceeding via an extended nucleation (up to 10% of the total reaction time) and size-focusing growth, for the whole length of the synthesis, thus enriching our understanding of the formation process. We identify the coordinating ligands (i.e., DOPA vs oleates) as the key parameter determining the stability of the Cs[$PbBr_3$] solutes present as 3 nm large dispersed agglomerates, responsible for slow nucleation and growth. Moreover, even with oleate ligands we show that dilution can result in slow growth with the emergence of a series of magic-sized NCs. We also observe the spontaneous organization of the NCs in the reaction vessel, resulting in three-dimensional face-centered orthorhombic superstructures and give a full description of the self-assembly process.

IN SITU TIME-RESOLVED SAXS: Cs-DOPA CASE

The synthesis was adopted from our recent report,[51] albeit for a 10−30 times higher overall concentration of all reagents (see the Supporting Information for further details). $PbBr_2$ solubilized in a hexane solution of TOPO was reacted with Cs-DOPA. The synthesis was monitored *in situ* by recording small-angle and wide-angle X-ray scattering (SAXS and WAXS) every 0.5 s (beamline P21.2 at Petra III (DESY) in Hamburg; X-ray energy of 37.5 keV). Interestingly, already 0.5 s after injection (Figure 1a) 3.0 nm small particles are present in high concentration, which we identify as agglomerates of Cs[$PbBr_3$] monomers. These species are characterized by the

https://doi.org/10.1021/acs.nanolett.2c04532
Nano Lett. 2023, 23, 667−676

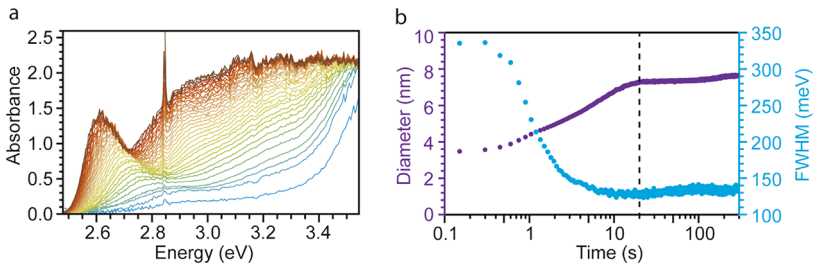

Figure 2. Monitoring nanocrystal growth by *in situ* optical absorbance spectroscopy. (a) Optical absorbance spectra collected during the synthesis of $CsPbBr_3$ NCs with a time resolution of 150 ms. (b) Temporal evolution of the mean NC size (purple), determined from the excitonic peak energy using the calibration curve from ref 14 and full width at half-maximum (fwhm) (light blue) of the first excitonic peak. The as-obtained NC sizes agree very well with those determined from SAXS fits (blue curve in Figure 1c). The dotted line at 20 s marks the transition from the growth phase to Ostwald ripening.

absorption band at 3.85 eV in ref 51, characteristic of zero-dimensional discrete $PbBr_3^-$ ions,[63,64] and might be solubilized by TOPO. *In situ* WAXS shows the amorphous nature of these species (Figure S4). Over time, a population of larger particles (starting with size 4.4 nm), henceforth referred to as NCs, steadily emerges, seen as defined minima on top of the scattering pattern of the $Cs[PbBr_3]$ agglomerates (dashed arrow in Figure 1a and Figure S3), accompanied by a reduction in the concentration of the monomer agglomerates. Hence, the agglomerates consisting of $Cs[PbBr_3]$ monomers and possibly coordinated by TOPO molecules serve as precursors for the subsequent nuclei.

From the final SAXS pattern, the average shape of the NCs was reconstructed (Figure 2b) by fitting the data with a shape-retrieval, dummy-atom-model based algorithm (see the Supporting Information); notably this fitting is performed without any prior assumption as to the shape of the scattering objects.[62] The average particle is characterized by a quasi-spherical shape and an average size of 8.1 nm. This retrieved NC shape is in accordance with our previous report on TOPO/$PbBr_2$ synthesis yielding rhombicuboctahedral-shaped NCs.[51] The crystal structure of the NCs is confirmed to be orthorhombic $CsPbBr_3$ (from WAXS, Figure S4; orthorhombic *Pbnm*, ICSD code 97851).

Four phases can be defined in the temporal evolution of the size, size distribution, concentration, and reaction yield (Figure 1c,d). In the first phase (t = 0.5 s, first recorded frame), the presence of 3.0 nm particles in high concentration was detected, showing that the conversion from $PbBr_2$ precursors to the $Cs[PbBr_3]$ agglomerates of solutes, which occurs faster than the time resolution of the measurement (0.5 s), matches with the conversion of roughly 100 ms recorded via *in situ* absorption.[51] In the second phase (t = 0.5−3 s), $CsPbBr_3$ NCs of a discrete size of 4.4 nm form, whose population increases at the expense of 3.0 nm $Cs[PbBr_3]$ agglomerates (Figure S5a). When the concentration of the 4.4 nm $CsPbBr_3$ NC peaks at 4.2 μM after 3 s (10% of the reaction time), the reaction enters the third phase (t = 3−30 s); here the 3.0 nm agglomerates are gradually depleted, while the 4.4 nm NCs grow at the expense of other (mostly smaller) NCs. In this phase, the NCs steadily decrease in number and polydispersity. The third phase concludes when the NC size plateaus at 7.4 nm, the polydispersity reaches a minimum of 0.70 nm (10% polydisperse; one $CsPbBr_3$ monolayer), and the reservoir of $Cs[PbBr_3]$ agglomerates is completely depleted (Figure S5a); in this phase the reaction reaches its final yield (61%). Interestingly, the total mass of the $Cs[PbBr_3]$ solutes converts almost completely into the mass of the NCs (Figure S5b). In the last phase (t > 30 s), a moderate increase in the NC size and size distribution, concomitantly with a moderate decrease in NC number, is indicative of Ostwald ripening.

IN SITU OPTICAL ABSORBANCE: Cs-DOPA CASE

The same synthesis was repeated while measuring, *in situ*, the optical absorbance (time resolution 150 ms; Figure 2), complementing the SAXS data. Interestingly, the first formed $CsPbBr_3$ NCs have an average size of 3.8 nm, slightly smaller than that obtained by SAXS. However, the broad absorption feature, our reliance on calibration curves to extract the particle diameter (especially for small particle size), and the fact that the calibration was based on cubic particles can account for this discrepancy. The growth of the NCs is accompanied by a strong decrease in the full width at half-maximum (fwhm) from 340 to 135 meV (phase II of SAXS). During the subsequent period of 7−20 s, the NC size continuously increases until it plateaus at 7.6 nm, while the fwhm remains constant at 135 meV, evidencing the size-focusing behavior observed also by SAXS (phase III of SAXS). For longer times (t > 20 s), the size and the fwhm slowly increase, as expected for Ostwald ripening (phase IV of SAXS). At the end of the reaction, the NC number concentration was measured (via *ex situ* optical absorbance; see the Supporting Information for details) to be 1.1 μM, in agreement with SAXS measurements (Figure S6). Overall, the evolution of the NC size as recorded by *in situ* absorbance (purple curve in Figure 2b) is in strong agreement with the same data recorded by *in situ* SAXS (blue curve in Figure 1c and Figure S7).

When repeating the same experiment in a more diluted (×2.5) regime (Figure S8), to achieve a much broader spectral range, a strong absorption feature at 3.9 eV appears immediately after the injection (250 ms). This can be attributed to the conversion of the Cs-DOPA and $PbBr_2$ precursors into $Cs[PbBr_3]$ agglomerates, as previously observed,[51,63,64] confirming our observations by means of SAXS.

ROLE OF THE COORDINATING LIGANDS: Cs-OA

The choice of coordinating ligand has a pivotal role in determining, among other things, the reaction kinetics and formation mechanism of NCs. In our synthesis, DOPA, introduced in the synthesis as Cs-DOPA, acts as a stabilizer for the obtained NCs, as follows from NMR (Figure S9). For comparison, we ran the synthesis substituting Cs-DOPA with Cs-oleate (Cs-OA) and acquired SAXS data. In contrast to the synthesis with Cs-DOPA, where the minima evidencing the

https://doi.org/10.1021/acs.nanolett.2c04532
Nano Lett. 2023, 23, 667−676

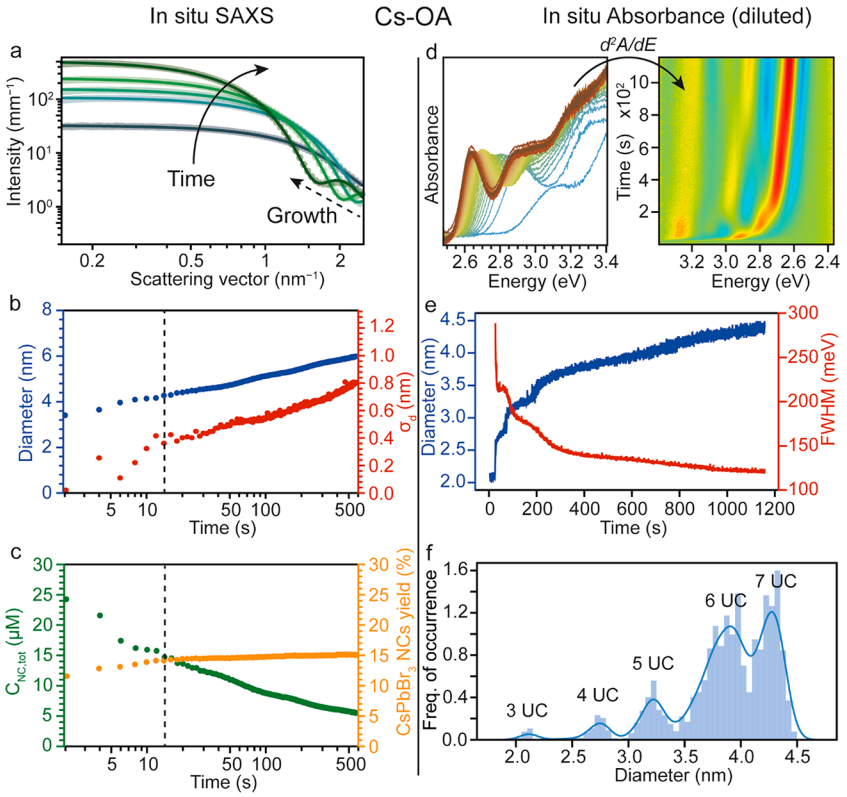

Figure 3. *In situ* time-resolved SAXS and optical absorbance measurements monitoring the evolution of the reaction using Cs-OA as the cationic reactant. (a) Five representative SAXS patterns (data points) collected during the formation of the nanocrystals, with their corresponding fits (solid lines). The patterns are collected at 2, 4, 12, 60, and 600 s, respectively. Over time the growth appears as a defined minimum shifting toward smaller values of the scattering vector **q**. (b) Average size (blue) and standard deviation (red) of the NC population as a function of the reaction time as extracted from the SAXS data. The dotted vertical line indicates the moment at which the reaction reaches its final yield. (c) Nanocrystal concentration (green) and $CsPbBr_3$ yield (orange) as a function of the reaction time. The dotted vertical line indicates the moment at which the reaction reaches its final yield. (d) (left) Optical absorbance spectra collected *in situ* during the synthesis of $CsPbBr_3$ NCs with Cs-OA (time resolution 100 ms). The peak associated with the first excitonic transition evolves over time, shifting toward lower energies, thus indicating NC growth. (right) Heat map representing the evolution over time of the second derivative of the absorption spectra, highlighting the discrete growth of the NCs over a series of very monodisperse (magic-sized) NCs. (e) Average size of the NCs (blue) as extracted from the position of the first excitonic peak and fwhm of the first excitonic peak (red) as a function of time. The abrupt shifts in both trends are symptomatic of the discrete growth of the NCs under these diluted conditions. (f) Histogram of the NC size as extracted from *in situ* absorption data over time using a calibration curve. The values above are the estimated diameters of the NCs in number of unit cells (UC), determined from the excitonic peak energy using the calibration curve from ref 14.

formation of NCs appeared at a specific value of the scattering vector (**q**), in this case the minima shift from larger to smaller values (dashed arrow in Figure 3a). The obtained NCs have a similar rounded shape and the same crystal structure (Figures S10 and S11) as in the Cs-DOPA case. Considering now the temporal evolution of the synthesis (Figure 3b,c), the first frame (2 s) shows the presence of $CsPbBr_3$ NCs in high concentrations (24 μM; ca. 3.4 nm in diameter; Figure S11) and the absence of any free $Cs[PbBr_3]$ agglomerates, evidencing a fast nucleation event (<2 s); at the same time, the reaction yield is ∼76% of its final value already at this early stage. The difference between the two syntheses becomes more evident at longer times (t > 2 s): for Cs-OA, the scattered signal originates from a single population of growing scattering objects, unlike that from the $Cs[PbBr_3]$ agglomerates and NC mixtures in the Cs-DOPA case. Furthermore, for the Cs-OA case, the NC growth is accompanied by a decrease in the NC concentration and widening of the size distribution. Compared to Cs-DOPA, where size focusing is observed, the synthesis with Cs-OA produces a mere translation of the size distribution over time, without size focusing. At t = 14 s, the reaction reaches its final yield; this is notably only ∼25% of the final yield observed when Cs-DOPA is used. At this point the reaction enters the Ostwald ripening phase. The absence of $Cs[PbBr_3]$ agglomerates and size focusing and the presence of a fast nucleation event (<250 ms) are confirmed by *in situ* optical absorbance (Figures S12 and S13).

However, when performing the synthesis in much more diluted solutions (35−45 times), the *in situ* absorbance points to discrete steps in the evolution of the NC size (as extracted from the position of the first excitonic peak, see Figure 3d).These are accompanied by abrupt drops in the fwhm of the first excitonic peak (Figure 3e). Furthermore, when producing a histogram of the NC sizes as extracted from each frame (100 ms), specific "magic-size" crystals can be identified (Figure 3f), showing that the growth occurs plane by plane, the intermediate NCs being very monodisperse and stable. In this respect, the intermediate magic-sized NCs strikingly remain the same when the reaction conditions such as dilution are altered to adjust the final NC size (Figure S14). Hence, dilution of the reactants vs the amount of oleic acid is a

https://doi.org/10.1021/acs.nanolett.2c04532
Nano Lett. 2023, 23, 667−676

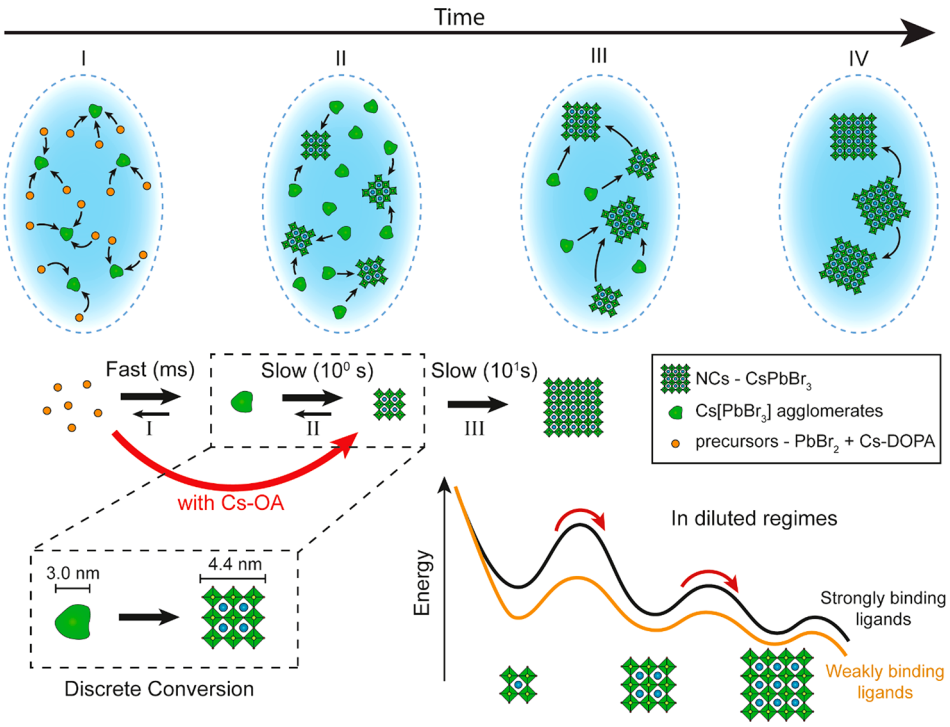

Figure 4. Schema showing the proposed formation mechanism for $CsPbBr_3$ NCs involving the appearance of stable $Cs[PbBr_3]$ agglomerates and size-focusing growth when weakly binding ligands are used (i.e., DOPA). The NC formation proceeds through four phases: (I) very fast (approximately milliseconds) formation of 3.0 nm amorphous $Cs[PbBr_3]$ agglomerates from $PbBr_2$ and Cs-DOPA precursors; (II) conversion of some 3.0 nm agglomerates into NCs with diameters as small as 4.4 nm (7 $CsPbBr_3$ unit cells), where the NC concentration reaches a maximum; (III) size-focusing growth of the NCs at the expense of the $Cs[PbBr_3]$ agglomerates and via coalescence or redissolution of some of the NCs, with complete depletion of the 3.0 nm $Cs[PbBr_3]$ agglomerates; (IV) Ostwald ripening causing size defocusing and decrease in NC concentration. The use of Cs-OA as a precursor prevents the stabilization of the $Cs[PbBr_3]$ agglomerates and size focusing. The occurrence of discrete growth in diluted regimes is enabled by the energetically consistent kinetic barriers between NCs of different size, originating from the presence, in solution, of strongly binding ligands (i.e., OA).

new and promising route to obtain highly monodisperse OA-capped $CsPbBr_3$ NCs of any size.

NUCLEATION AND DISCRETE GROWTH MECHANISM

The *in situ* optical absorbance and SAXS results presented above, together with our former study on the same system at much higher dilution levels,[51] point to the following mechanism of NC formation (Figure 4). First, $PbBr_2$ and Cs-DOPA rapidly convert into 3.0 nm amorphous agglomerates, consisting of $Cs[PbBr_3]$ monomers; this occurs on a sub-millisecond scale (phase I). Subsequently, some of these agglomerates convert into 4.4 nm $CsPbBr_3$ NCs within seconds (phase II). The $CsPbBr_3$ NCs continue growing at the expense of the amorphous agglomerates and the smaller NCs (phase III), followed by Ostwald ripening (phase IV). We hypothesize that the binding affinity of the DOPA ligand in this room-temperature synthesis is key for observing size focusing. Specifically, the weakly binding DOPA ligands allow the formation of $Cs[PbBr_3]$ agglomerates. As these agglomerates "store" the $Cs[PbBr_3]$ monomers and keep them out of the solution, they slow down nucleation and growth. As previously shown,[38,51] DOPA is a weak ligand to all lead bromide species; hence, it inherently stabilizes the formation of $Cs[PbBr_3]$ monomers that agglomerate. Under these synthesis conditions, the conversion of these agglomerates of monomers into 4.4 nm NCs is much slower than that of the precursors into agglomerates. Hence, the temporal evolution of the agglomerates' mass and the $CsPbBr_3$ NCs' mass have the same kinetics (Figure S5b). Therefore, the low monomer concentration in solution limits the rate of nucleation and growth, in a complementary way as previously observed in highly diluted systems.[51] The slow release of $Cs[PbBr_3]$ monomers results in an extended nucleation event (up to 10% of the total reaction time; phase II), followed by slow and size-focusing growth (phase III). In stark contrast, when conventional strongly binding OA molecules are used,[44] the stability of the $Cs[PbBr_3]$ is compromised (i.e., $Pb(OA)_2$ is more stable than $Pb(DOPA)_2$) and the formation of the NCs proceeds through a burst event (few milliseconds) and size defocusing.

In highly diluted regimes (concentration of deficient species ca. 9×10^{-5} M), the presence of strong binding ligands (OA) on the surface of the NCs gives origin to atomically discrete NC growth, as the energetically consistent kinetic barrier separating NCs of different size reflects the amount of energy required to remove a ligand and adsorb a new monomer.

SPONTANEOUS ASSEMBLY OF LEAD HALIDE PEROVSKITE NCS IN THE REACTION VESSEL

Polydispersity of the NC size distribution and the choice of the ligand shell and the solvent (i.e., the strength of the interparticle forces) have a pivotal role in the interactions between NCs and NC self-assembly.[65] When performing the synthesis at 100 °C with Cs-DOPA as a precursor, we observe, by means of *in situ* SAXS and in contrast to when Cs-OA is used (Figure S15), the appearance of sharp structure factor

https://doi.org/10.1021/acs.nanolett.2c04532
Nano Lett. 2023, 23, 667−676

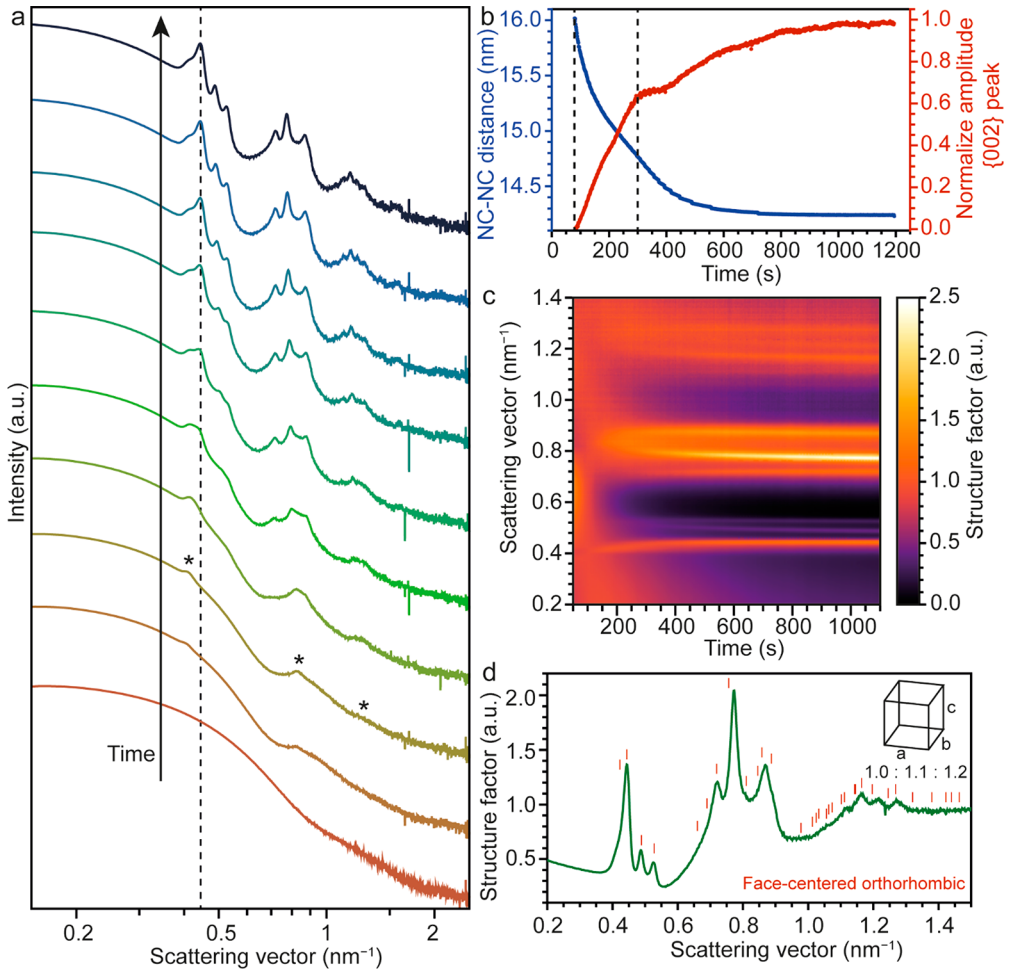

Figure 5. Self-assembly of lead halide perovskite NCs in solution. (a) SAXS patterns collected at different times (from the bottom to the top: 10, 90, 105, 200, 280, 420, 520, 680, 900, and 1200 s) during the spontaneous self-assembly of lead halide perovskite NCs in solution and shifted for clarity. The appearance of peaks at 0.39, 0.80, and 1.20 nm^{-1}, indicating the alignment of NCs into one direction, after 90 s from the beginning of the reaction is highlighted by asterisks. Over time the peaks evolve into sharp structure factor peaks. The dotted line is a guide to appreciate the shift of the {002} structure peak toward higher values of **q** over time. (b) Evolution of the NC−NC distance (blue) and average amplitude of the {002} peak (red) over time. The two dotted lines highlight respectively the beginning of the crystallization (left line) at 90 s and the splitting of the three periodic peaks into multiple structure factor peaks (right line) after 300 s. (c) Heat map representing the evolution of the structure factor as a function of time. (d) Structure factor of the last recorded frame at 1100 s. The red ticks indicate the reference reflections of a face-centered orthorhombic crystal with aspect ratio 1.0:1.1:1.2.

peaks, indicating the spontaneous formation of superstructures[11,13,66] in the reaction vessel (Figure 5a). In the first 90 s of the reaction, the average NC diameter steadily grows to a value of 11.6 nm, comparable to the synthesis with Cs-OA (Figure S15). At this critical size, structure factor peaks arise at 0.39, 0.80, and 1.20 nm^{-1}, which become sharper over time. The periodicity of the peaks suggests that the interparticle forces drive the NCs to assemble in a one-dimensional structure with a periodicity, or center-to-center distance, of 16.0 nm, similar to earlier observations with CdSe nanoplatelets.[67] We suggest that the self-assembly into 1D structures is induced by the selective attachment of DOPA ligands to specific facets of the rhombocubioctahedral LHP NCs that are differently terminated. Over time, the NC−NC distance decreases (blue in Figure 5b) as the NCs are pulled together and their ligands start to interpenetrate; at the same time, the increase in sharpness of the first structure peak (red in Figure 5b) suggests that the average size of the one-dimensional superstructures is still increasing. 300 s into the reaction, the three periodic peaks evolve into multiple structure factor peaks whose amplitude and position change over time (Figure 5c). This suggests that the different one-dimensional superstructures combine to form a three-dimensional superstructure, as observed e.g. when semiconductor nanoplatelets are destabilized by the addition of an antisolvent.[67] Notably, the three-dimensional crystallization happens when the NCs have an average NC−NC distance of 14.8 nm, hence with a surface-to-surface distance of 3.2 nm. At this surface-to-surface distance, van der Waals attractions can trigger the superstructure crystallization. This is consistent with previous observations of spontaneous crystallization triggered by interparticle interactions.[59,68−70]

By analyzing the last frame of the structure factor, we can determine that the crystal structure in which the LHP NCs self-assemble is face-centered orthorhombic (Figure 5d) with crystal lattice parameters *a*, *b*, and *c* of, respectively, 14.6, 16.0, and 17.8 nm, corresponding to an aspect ratio of 1.0:1.1:1.2. NCs of these sizes typically pack into face-centered-cubic or hexagonal-close-packed structures, which are the most favorable packing structures for spheres,[71,72] as these structures

https://doi.org/10.1021/acs.nanolett.2c04532
Nano Lett. 2023, 23, 667−676

are favored by the entropy-driven assembly and the interparticle interactions. However, since our particles are quasi-spherical (as determined from particle reconstruction, Figure 1b), their self-assembly results in a distorted face-centered cubic, hence face-centered orthorhombic, structure with an aspect ratio close to 1.0. The final size of the superstructures, as extracted from the fwhm of the SAXS data using the Scherrer equation $\left(\text{crystal size} \approx \frac{2\pi}{\text{FWHM}}\right)$, is ∼300 nm.

In summary, we investigated the formation of $CsPbBr_3$ NCs in a TOPO/$PbBr_2$ synthesis,[51] recently reported to provide monodisperse NCs in a broad size range, by means of *in situ* SAXS and optical absorbance. The experimental evidence collected during the synthesis, which resulted in NCs with a highly monodisperse size distribution already in the crude product, allowed us to determine a general formation mechanism for this system, proceeding via extended nucleation events (3 s, ∼10% of growth time) and size-focusing growth. We identify dispersed agglomerates of $Cs[PbBr_3]$ monomers as the key intermediate species: they preclude the nucleation of NCs and slowly release $Cs[PbBr_3]$ monomers for further growth. Hence, the $Cs[PbBr_3]$ intermediate concentration is a key parameter in the reaction. This is also illustrated in the more commonly used synthesis with strongly binding OA ligands by simply diluting the reactants. Moreover, when the synthesis was performed at high temperatures (100 °C), spontaneous self-assembly of the NCs into three-dimensional superstructures was observed when the NCs reached a critical size of 11.6 nm. Via a quantitative analysis of the scattering data over time, we determined the self-assembly mechanism, which proceeds first via the formation of one-dimensional superstructures, which later combine to form a three-dimensional NC lattice. The final crystal structure was identified as face-centered orthorhombic with a crystal cell of aspect ratio ∼1.0.

■ ASSOCIATED CONTENT

Supporting Information

The Supporting Information is available free of charge at https://pubs.acs.org/doi/10.1021/acs.nanolett.2c04532.

Synthetic procedure for $CsPbBr_3$ nanocrystals, *in situ* analysis by SAXS and optical absorption, data analysis of SAXS patterns, *in situ* WAXS data, and characterization methods (PDF)

■ AUTHOR INFORMATION

Corresponding Authors

Federico Montanarella − *Laboratory of Inorganic Chemistry, Department of Chemistry and Applied Biosciences, ETH Zürich, CH-8093 Zürich, Switzerland; Laboratory for Thin Films and Photovoltaics, Empa − Swiss Federal Laboratories for Materials Science and Technology, CH-8600 Dübendorf, Switzerland;* Present Address: Seaborough BV, Matrix VII Innovation Center, Science Park 106, 1098 XG Amsterdam, The Netherlands; orcid.org/0000-0002-9057-7414; Email: f.montanarella@seaborough.com

Maksym V. Kovalenko − *Laboratory of Inorganic Chemistry, Department of Chemistry and Applied Biosciences, ETH Zürich, CH-8093 Zürich, Switzerland; Laboratory for Thin Films and Photovoltaics, Empa − Swiss Federal Laboratories for Materials Science and Technology, CH-8600 Dübendorf, Switzerland;* orcid.org/0000-0002-6396-8938; Email: mvkovalenko@ethz.ch

Authors

Quinten A. Akkerman − *Laboratory of Inorganic Chemistry, Department of Chemistry and Applied Biosciences, ETH Zürich, CH-8093 Zürich, Switzerland; Laboratory for Thin Films and Photovoltaics, Empa − Swiss Federal Laboratories for Materials Science and Technology, CH-8600 Dübendorf, Switzerland;* Present Address: Lehrstuhl für Photonik und Optoelektronik, Nano-Institut München und Fakultät für Physik, Ludwig-Maximilians-Universität (LMU), Königinstr. 10, D-80539 München, Germany; orcid.org/0000-0002-8699-9390

Dennis Bonatz − *Institute of Physical Chemistry, University of Hamburg, 20146 Hamburg, Germany*

Maaike M. van der Sluijs − *Debye Institute for Nanomaterials Science, Utrecht University, 3584 CC Utrecht, The Netherlands;* orcid.org/0000-0001-7097-5506

Johanna C. van der Bok − *Debye Institute for Nanomaterials Science, Utrecht University, 3584 CC Utrecht, The Netherlands;* orcid.org/0000-0002-1810-3513

P. Tim Prins − *Debye Institute for Nanomaterials Science, Utrecht University, 3584 CC Utrecht, The Netherlands;* orcid.org/0000-0002-8258-0074

Marcel Aebli − *Laboratory of Inorganic Chemistry, Department of Chemistry and Applied Biosciences, ETH Zürich, CH-8093 Zürich, Switzerland; Laboratory for Thin Films and Photovoltaics, Empa − Swiss Federal Laboratories for Materials Science and Technology, CH-8600 Dübendorf, Switzerland*

Alf Mews − *Institute of Physical Chemistry, University of Hamburg, 20146 Hamburg, Germany*

Daniel Vanmaekelbergh − *Debye Institute for Nanomaterials Science, Utrecht University, 3584 CC Utrecht, The Netherlands;* orcid.org/0000-0002-3535-8366

Complete contact information is available at: https://pubs.acs.org/10.1021/acs.nanolett.2c04532

Notes

The authors declare no competing financial interest.

■ ACKNOWLEDGMENTS

F.M. acknowledges support from ETH Zürich via an ETH Postdoctoral Fellowship (FEL-15 18-2) and from the Marie Sklodowska-Curie Actions COFUND Program. F.M. also acknowledges financial support from the European Union's Horizon 2020 program, through a FET Open research and innovation action under the grant agreement No. 899141 (PoLLoC). This research was carried out at beamline P21.2 at PETRA III at DESY, a member of the Helmholtz Association (HGF). The authors thank Dr. Malte Blankenburg and Dr. Ulrich Lienert for assistance during the experiment. The research leading to this result has been supported by the project CALIPSOplus under the Grant Agreement 730872 from the EU Framework Programme for Research and Innovation HORIZON 2020. D.B. acknowledges financial support from the Cluster of Excellence "CUI: Advanced Imaging of Matter" of the Deutsche Forschungsgemeinschaft (DFG) - EXC 2056 - project ID 390715994.

REFERENCES

(1) Protesescu, L.; Yakunin, S.; Bodnarchuk, M. I.; Krieg, F.; Caputo, R.; Hendon, C. H.; Yang, R. X.; Walsh, A.; Kovalenko, M. V. Nanocrystals of Cesium Lead Halide Perovskites ($CsPbX_3$, X = Cl, Br, and I): Novel Optoelectronic Materials Showing Bright Emission with Wide Color Gamut. *Nano Lett.* **2015**, *15* (6), 3692−3696.

(2) Kovalenko, M. V.; Bodnarchuk, M. I. Lead Halide Perovskite Nanocrystals: From Discovery to Self-Assembly and Applications. *Chimia (Aarau)* **2017**, *71* (7−8), 461−470.

(3) Kovalenko, M. V.; Protesescu, L.; Bodnarchuk, M. I. Properties and Potential Optoelectronic Applications of Lead Halide Perovskite Nanocrystals. *Science* **2017**, *358* (6364), 745−750.

(4) Akkerman, Q. A.; Rainò, G.; Kovalenko, M. V.; Manna, L. Genesis, Challenges and Opportunities for Colloidal Lead Halide Perovskite Nanocrystals. *Nat. Mater.* **2018**, *17* (5), 394−405.

(5) Huang, H.; Bodnarchuk, M. I.; Kershaw, S. V.; Kovalenko, M. V.; Rogach, A. L. Lead Halide Perovskite Nanocrystals in the Research Spotlight: Stability and Defect Tolerance. *ACS Energy Lett.* **2017**, *2* (9), 2071−2083.

(6) Dey, A.; Ye, J.; De, A.; Debroye, E.; Ha, S. K.; Bladt, E.; Kshirsagar, A. S.; Wang, Z.; Yin, J.; Wang, Y.; Quan, L. N.; Yan, F.; Gao, M.; Li, X.; Shamsi, J.; Debnath, T.; Cao, M.; Scheel, M. A.; Kumar, S.; Steele, J. A.; Gerhard, M.; Chouhan, L.; Xu, K.; Wu, X.; Li, Y.; Zhang, Y.; Dutta, A.; Han, C.; Vincon, I.; Rogach, A. L.; Nag, A.; Samanta, A.; Korgel, B. A.; Shih, C.; Gamelin, D. R.; Son, D. H.; Zeng, H.; Zhong, H.; Sun, H.; Demir, H. V.; Scheblykin, I. G.; Mora-Seró, I.; Stolarczyk, J. K.; Zhang, J. Z.; Feldmann, J.; Hofkens, J.; Luther, J. M.; Pérez-Prieto, J.; Li, L.; Manna, L.; Bodnarchuk, M. I.; Kovalenko, M. V.; Roeffaers, M. B. J.; Pradhan, N.; Mohammed, O. F.; Bakr, O. M.; Yang, P.; Müller-Buschbaum, P.; Kamat, P. V.; Bao, Q.; Zhang, Q.; Krahne, R.; Galian, R. E.; Stranks, S. D.; Bals, S.; Biju, V.; Tisdale, W. A.; Yan, Y.; Hoye, R. L. Z.; Polavarapu, L. State of the Art and Prospects for Halide Perovskite Nanocrystals. *ACS Nano* **2021**, *15* (7), 10775−10981.

(7) Becker, M. A.; Vaxenburg, R.; Nedelcu, G.; Sercel, P. C.; Shabaev, A.; Mehl, M. J.; Michopoulos, J. G.; Lambrakos, S. G.; Bernstein, N.; Lyons, J. L.; Stöferle, T.; Mahrt, R. F.; Kovalenko, M. V.; Norris, D. J.; Rainò, G.; Efros, A. L. Bright Triplet Excitons in Caesium Lead Halide Perovskites. *Nature* **2018**, *553* (7687), 189−193.

(8) Rainò, G.; Nedelcu, G.; Protesescu, L.; Bodnarchuk, M. I.; Kovalenko, M. V.; Mahrt, R. F.; Stöferle, T. Single Cesium Lead Halide Perovskite Nanocrystals at Low Temperature: Fast Single-Photon Emission, Reduced Blinking, and Exciton Fine Structure. *ACS Nano* **2016**, *10* (2), 2485−2490.

(9) Park, Y.-S.; Guo, S.; Makarov, N. S.; Klimov, V. I. Room Temperature Single-Photon Emission from Individual Perovskite Quantum Dots. *ACS Nano* **2015**, *9* (10), 10386−10393.

(10) Hu, F.; Zhang, H.; Sun, C.; Yin, C.; Lv, B.; Zhang, C.; Yu, W. W.; Wang, X.; Zhang, Y.; Xiao, M. Superior Optical Properties of Perovskite Nanocrystals as Single Photon Emitters. *ACS Nano* **2015**, *9* (12), 12410−12416.

(11) Rainò, G.; Becker, M. A.; Bodnarchuk, M. I.; Mahrt, R. F.; Kovalenko, M. V.; Stöferle, T. Superfluorescence from Lead Halide Perovskite Quantum Dot Superlattices. *Nature* **2018**, *563* (7733), 671−675.

(12) Rainò, G.; Utzat, H.; Bawendi, M. G.; Kovalenko, M. V. Superradiant Emission from Self-Assembled Light Emitters: From Molecules to Quantum Dots. *MRS Bull.* **2020**, *45* (10), 841−848.

(13) Tong, Y.; Yao, E.; Manzi, A.; Bladt, E.; Wang, K.; Döblinger, M.; Bals, S.; Müller-Buschbaum, P.; Urban, A. S.; Polavarapu, L.; Feldmann, J. Spontaneous Self-Assembly of Perovskite Nanocrystals into Electronically Coupled Supercrystals: Toward Filling the Green Gap. *Adv. Mater.* **2018**, *30* (29), 1801117.

(14) Krieg, F.; Sercel, P. C.; Burian, M.; Andrusiv, H.; Bodnarchuk, M. I.; Stöferle, T.; Mahrt, R. F.; Naumenko, D.; Amenitsch, H.; Rainò, G.; Kovalenko, M. v. Monodisperse Long-Chain Sulfobetaine-Capped $CsPbBr_3$ Nanocrystals and Their Superfluorescent Assemblies. *ACS Cent Sci.* **2021**, *7* (1), 135−144.

(15) Vila-Liarte, D.; Feil, M. W.; Manzi, A.; Garcia-Pomar, J. L.; Huang, H.; Döblinger, M.; Liz-Marzán, L. M.; Feldmann, J.; Polavarapu, L.; Mihi, A. Templated-Assembly of $CsPbBr_3$ Perovskite Nanocrystals into 2D Photonic Supercrystals with Amplified Spontaneous Emission. *Angew. Chem., Int. Ed.* **2020**, *59* (40), 17750−17756.

(16) Li, X.; Wu, Y.; Zhang, S.; Cai, B.; Gu, Y.; Song, J.; Zeng, H. $CsPbX_3$ Quantum Dots for Lighting and Displays: Room-Temperature Synthesis, Photoluminescence Superiorities, Underlying Origins and White Light-Emitting Diodes. *Adv. Funct Mater.* **2016**, *26* (15), 2435−2445.

(17) Liu, P.; Chen, W.; Wang, W.; Xu, B.; Wu, D.; Hao, J.; Cao, W.; Fang, F.; Li, Y.; Zeng, Y.; Pan, R.; Chen, S.; Cao, W.; Sun, X. W.; Wang, K. Halide-Rich Synthesized Cesium Lead Bromide Perovskite Nanocrystals for Light-Emitting Diodes with Improved Performance. *Chem. Mater.* **2017**, *29* (12), 5168−5173.

(18) Yan, F.; Xing, J.; Xing, G.; Quan, L.; Tan, S. T.; Zhao, J.; Su, R.; Zhang, L.; Chen, S.; Zhao, Y.; Huan, A.; Sargent, E. H.; Xiong, Q.; Demir, H. V. Highly Efficient Visible Colloidal Lead-Halide Perovskite Nanocrystal Light-Emitting Diodes. *Nano Lett.* **2018**, *18* (5), 3157−3164.

(19) Wang, H.-C.; Lin, S.-Y.; Tang, A.-C.; Singh, B. P.; Tong, H.-C.; Chen, C.-Y.; Lee, Y.-C.; Tsai, T.-L.; Liu, R.-S. Mesoporous Silica Particles Integrated with All-Inorganic $CsPbBr_3$ Perovskite Quantum-Dot Nanocomposites (MP-PQDs) with High Stability and Wide Color Gamut Used for Backlight Display. *Angew. Chem., Int. Ed.* **2016**, *55* (28), 7924−7929.

(20) Liu, M.; Zhong, G.; Yin, Y.; Miao, J.; Li, K.; Wang, C.; Xu, X.; Shen, C.; Meng, H. Aluminum-Doped Cesium Lead Bromide Perovskite Nanocrystals with Stable Blue Photoluminescence Used for Display Backlight. *Advanced Science* **2017**, *4* (11), 1700335.

(21) Yoon, H. C.; Kang, H.; Lee, S.; Oh, J. H.; Yang, H.; Do, Y. R. Study of Perovskite QD Down-Converted LEDs and Six-Color White LEDs for Future Displays with Excellent Color Performance. *ACS Appl. Mater. Interfaces* **2016**, *8* (28), 18189−18200.

(22) Chen, Q.; Wu, J.; Ou, X.; Huang, B.; Almutlaq, J.; Zhumekenov, A. A.; Guan, X.; Han, S.; Liang, L.; Yi, Z.; Li, J.; Xie, X.; Wang, Y.; Li, Y.; Fan, D.; Teh, D. B. L.; All, A. H.; Mohammed, O. F.; Bakr, O. M.; Wu, T.; Bettinelli, M.; Yang, H.; Huang, W.; Liu, X. All-Inorganic Perovskite Nanocrystal Scintillators. *Nature* **2018**, *561* (7721), 88−93.

(23) Zhang, Y.; Sun, R.; Ou, X.; Fu, K.; Chen, Q.; Ding, Y.; Xu, L.-J.; Liu, L.; Han, Y.; Malko, A. V.; Liu, X.; Yang, H.; Bakr, O. M.; Liu, H.; Mohammed, O. F. Metal Halide Perovskite Nanosheet for X-Ray High-Resolution Scintillation Imaging Screens. *ACS Nano* **2019**, *13* (2), 2520−2525.

(24) Heo, J. H.; Shin, D. H.; Park, J. K.; Kim, D. H.; Lee, S. J.; Im, S. H. High-Performance Next-Generation Perovskite Nanocrystal Scintillator for Nondestructive X-Ray Imaging. *Adv. Mater.* **2018**, *30* (40), 1801743.

(25) Yakunin, S.; Sytnyk, M.; Kriegner, D.; Shrestha, S.; Richter, M.; Matt, G. J.; Azimi, H.; Brabec, C. J.; Stangl, J.; Kovalenko, M. V.; Heiss, W. Detection of X-Ray Photons by Solution-Processed Lead Halide Perovskites. *Nat. Photonics* **2015**, *9* (7), 444−449.

(26) Wei, H.; Huang, J. Halide Lead Perovskites for Ionizing Radiation Detection. *Nat. Commun.* **2019**, *10* (1), 1066.

(27) Yakunin, S.; Dirin, D. N.; Shynkarenko, Y.; Morad, V.; Cherniukh, I.; Nazarenko, O.; Kreil, D.; Nauser, T.; Kovalenko, M. V. Detection of Gamma Photons Using Solution-Grown Single Crystals of Hybrid Lead Halide Perovskites. *Nat. Photonics* **2016**, *10* (9), 585−589.

(28) McCall, K. M.; Sakhatskyi, K.; Lehmann, E.; Walfort, B.; Losko, A. S.; Montanarella, F.; Bodnarchuk, M. I.; Krieg, F.; Kelestemur, Y.; Mannes, D.; Shynkarenko, Y.; Yakunin, S.; Kovalenko, M. V. Fast Neutron Imaging with Semiconductor Nanocrystal Scintillators. *ACS Nano* **2020**, *14* (11), 14686−14697.

(29) Montanarella, F.; McCall, K. M.; Sakhatskyi, K.; Yakunin, S.; Trtik, P.; Bernasconi, C.; Cherniukh, I.; Mannes, D.; Bodnarchuk, M. I.; Strobl, M.; Walfort, B.; Kovalenko, M. V. Highly Concentrated,

https://doi.org/10.1021/acs.nanolett.2c04532
Nano Lett. 2023, 23, 667−676

Zwitterionic Ligand-Capped Mn^{2+}:$CsPb(BrxCl_{1-x})_3$ Nanocrystals as Bright Scintillators for Fast Neutron Imaging. *ACS Energy Lett.* **2021**, *6* (12), 4365−4373.
(30) Yakunin, S.; Chaaban, J.; Benin, B. M.; Cherniukh, I.; Bernasconi, C.; Landuyt, A.; Shynkarenko, Y.; Bolat, S.; Hofer, C.; Romanyuk, Y. E.; Cattaneo, S.; Pokutnyi, S. I.; Schaller, R. D.; Bodnarchuk, M. I.; Poulikakos, D.; Kovalenko, M. V. Radiative Lifetime-Encoded Unicolour Security Tags Using Perovskite Nanocrystals. *Nat. Commun.* **2021**, *12* (1), 981.
(31) Liu, Y.; Zheng, Y.; Zhu, Y.; Ma, F.; Zheng, X.; Yang, K.; Zheng, X.; Xu, Z.; Ju, S.; Zheng, Y.; Guo, T.; Qian, L.; Li, F. Unclonable Perovskite Fluorescent Dots with Fingerprint Pattern for Multilevel Anticounterfeiting. *ACS Appl. Mater. Interfaces* **2020**, *12* (35), 39649−39656.
(32) Krieg, F.; Ochsenbein, S. T.; Yakunin, S.; ten Brinck, S.; Aellen, P.; Süess, A.; Clerc, B.; Guggisberg, D.; Nazarenko, O.; Shynkarenko, Y.; Kumar, S.; Shih, C.-J.; Infante, I.; Kovalenko, M. V. Colloidal $CsPbX_3$ (X = Cl, Br, I) Nanocrystals 2.0: Zwitterionic Capping Ligands for Improved Durability and Stability. *ACS Energy Lett.* **2018**, *3* (3), 641−646.
(33) Krieg, F.; Ong, Q. K.; Burian, M.; Rainò, G.; Naumenko, D.; Amenitsch, H.; Süess, A.; Grotevent, M. J.; Krumeich, F.; Bodnarchuk, M. I.; Shorubalko, I.; Stellacci, F.; Kovalenko, M. V. Stable Ultraconcentrated and Ultradilute Colloids of $CsPbX_3$ (X = Cl, Br) Nanocrystals Using Natural Lecithin as a Capping Ligand. *J. Am. Chem. Soc.* **2019**, *141* (50), 19839−19849.
(34) Wang, Y.-K.; Ma, D.; Yuan, F.; Singh, K.; Pina, J. M.; Johnston, A.; Dong, Y.; Zhou, C.; Chen, B.; Sun, B.; Ebe, H.; Fan, J.; Sun, M.-J.; Gao, Y.; Lu, Z.-H.; Voznyy, O.; Liao, L.-S.; Sargent, E. H. Chelating-Agent-Assisted Control of CsPbBr3 Quantum Well Growth Enables Stable Blue Perovskite Emitters. *Nat. Commun.* **2020**, *11* (1), 3674.
(35) Dong, Y.; Wang, Y.-K.; Yuan, F.; Johnston, A.; Liu, Y.; Ma, D.; Choi, M.-J.; Chen, B.; Chekini, M.; Baek, S.-W.; Sagar, L. K.; Fan, J.; Hou, Y.; Wu, M.; Lee, S.; Sun, B.; Hoogland, S.; Quintero-Bermudez, R.; Ebe, H.; Todorovic, P.; Dinic, F.; Li, P.; Kung, H. T.; Saidaminov, M. I.; Kumacheva, E.; Spiecker, E.; Liao, L.-S.; Voznyy, O.; Lu, Z.-H.; Sargent, E. H. Bipolar-Shell Resurfacing for Blue LEDs Based on Strongly Confined Perovskite Quantum Dots. *Nat. Nanotechnol* **2020**, *15* (8), 668−674.
(36) Dhanabalan, B.; Biffi, G.; Moliterni, A.; Olieric, V.; Giannini, C.; Saleh, G.; Ponet, L.; Prato, M.; Imran, M.; Manna, L.; Krahne, R.; Artyukhin, S.; Arciniegas, M. P. Engineering the Optical Emission and Robustness of Metal-Halide Layered Perovskites through Ligand Accommodation. *Adv. Mater.* **2021**, *33* (13), 2008004.
(37) Zhang, B.; Goldoni, L.; Lambruschini, C.; Moni, L.; Imran, M.; Pianetti, A.; Pinchetti, V.; Brovelli, S.; De Trizio, L.; Manna, L. Stable and Size Tunable $CsPbBr_3$ Nanocrystals Synthesized with Oleylphosphonic Acid. *Nano Lett.* **2020**, *20* (12), 8847−8853.
(38) Shynkarenko, Y.; Bodnarchuk, M. I.; Bernasconi, C.; Berezovska, Y.; Verteletskyi, V.; Ochsenbein, S. T.; Kovalenko, M. V. Direct Synthesis of Quaternary Alkylammonium-Capped Perovskite Nanocrystals for Efficient Blue and Green Light-Emitting Diodes. *ACS Energy Lett.* **2019**, *4* (11), 2703−2711.
(39) Bodnarchuk, M. I.; Boehme, S. C.; ten Brinck, S.; Bernasconi, C.; Shynkarenko, Y.; Krieg, F.; Widmer, R.; Aeschlimann, B.; Günther, D.; Kovalenko, M. V.; Infante, I. Rationalizing and Controlling the Surface Structure and Electronic Passivation of Cesium Lead Halide Nanocrystals. *ACS Energy Lett.* **2019**, *4* (1), 63−74.
(40) Imran, M.; Ijaz, P.; Baranov, D.; Goldoni, L.; Petralanda, U.; Akkerman, Q.; Abdelhady, A. L.; Prato, M.; Bianchini, P.; Infante, I.; Manna, L. Shape-Pure, Nearly Monodispersed $CsPbBr_3$ Nanocubes Prepared Using Secondary Aliphatic Amines. *Nano Lett.* **2018**, *18* (12), 7822−7831.
(41) Almeida, G.; Goldoni, L.; Akkerman, Q.; Dang, Z.; Khan, A. H.; Marras, S.; Moreels, I.; Manna, L. Role of Acid−Base Equilibria in the Size, Shape, and Phase Control of Cesium Lead Bromide Nanocrystals. *ACS Nano* **2018**, *12* (2), 1704−1711.
(42) Brown, A. A. M.; Vashishtha, P.; Hooper, T. J. N.; Ng, Y. F.; Nutan, G. V.; Fang, Y.; Giovanni, D.; Tey, J. N.; Jiang, L.; Damodaran, B.; Sum, T. C.; Pu, S. H.; Mhaisalkar, S. G.; Mathews, N. Precise Control of $CsPbBr_3$ Perovskite Nanocrystal Growth at Room Temperature: Size Tunability and Synthetic Insights. *Chem. Mater.* **2021**, *33* (7), 2387−2397.
(43) Zhang, B.; Goldoni, L.; Zito, J.; Dang, Z.; Almeida, G.; Zaccaria, F.; de Wit, J.; Infante, I.; De Trizio, L.; Manna, L. Alkyl Phosphonic Acids Deliver $CsPbBr_3$ Nanocrystals with High Photoluminescence Quantum Yield and Truncated Octahedron Shape. *Chem. Mater.* **2019**, *31* (21), 9140−9147.
(44) Almeida, G.; Ashton, O. J.; Goldoni, L.; Maggioni, D.; Petralanda, U.; Mishra, N.; Akkerman, Q. A.; Infante, I.; Snaith, H. J.; Manna, L. The Phosphine Oxide Route toward Lead Halide Perovskite Nanocrystals. *J. Am. Chem. Soc.* **2018**, *140* (44), 14878−14886.
(45) Prins, P. T.; Montanarella, F.; Dümbgen, K.; Justo, Y.; van der Bok, J. C.; Hinterding, S. O. M.; Geuchies, J. J.; Maes, J.; De Nolf, K.; Deelen, S.; Meijer, H.; Zinn, T.; Petukhov, A. V.; Rabouw, F. T.; De Mello Donega, C.; Vanmaekelbergh, D.; Hens, Z. Extended Nucleation and Superfocusing in Colloidal Semiconductor Nanocrystal Synthesis. *Nano Lett.* **2021**, *21* (6), 2487−2496.
(46) van der Bok, J. C.; Prins, P. T.; Montanarella, F.; Maaskant, D. N.; Brzesowsky, F. A.; van der Sluijs, M. M.; Salzmann, B. B. v.; Rabouw, F. T.; Petukhov, A. v.; de Mello Donega, C.; Vanmaekelbergh, D.; Meijerink, A. *In Situ* Optical and X-Ray Spectroscopy Reveals Evolution toward Mature CdSe Nanoplatelets by Synergetic Action of Myristate and Acetate Ligands. *J. Am. Chem. Soc.* **2022**, *144* (18), 8096−8105.
(47) Lignos, I.; Stavrakis, S.; Nedelcu, G.; Protesescu, L.; DeMello, A. J.; Kovalenko, M. V. Synthesis of Cesium Lead Halide Perovskite Nanocrystals in a Droplet-Based Microfluidic Platform: Fast Parametric Space Mapping. *Nano Lett.* **2016**, *16* (3), 1869−1877.
(48) Lignos, I.; Morad, V.; Shynkarenko, Y.; Bernasconi, C.; Maceiczyk, R. M.; Protesescu, L.; Bertolotti, F.; Kumar, S.; Ochsenbein, S. T.; Masciocchi, N.; Guagliardi, A.; Shih, C.-J.; Bodnarchuk, M. I.; DeMello, A. J.; Kovalenko, M. V. Exploration of Near-Infrared-Emissive Colloidal Multinary Lead Halide Perovskite Nanocrystals Using an Automated Microfluidic Platform. *ACS Nano* **2018**, *12* (6), 5504−5517.
(49) Peng, X.; Wickham, J.; Alivisatos, A. P. Kinetics of II-VI and III-V Colloidal Semiconductor Nanocrystal Growth: "Focusing" of Size Distributions. *J. Am. Chem. Soc.* **1998**, *120* (21), 5343−5344.
(50) Qu, L.; Yu, W. W.; Peng, X. In Situ Observation of the Nucleation and Growth of CdSe Nanocrystals. *Nano Lett.* **2004**, *4* (3), 465−469.
(51) Akkerman, Q. A.; Nguyen, T. P. T.; Boehme, S. C.; Montanarella, F.; Dirin, D. N.; Wechsler, P.; Beiglböck, F.; Rainò, G.; Erni, R.; Katan, C.; Even, J.; Kovalenko, M. v. Controlling the Nucleation and Growth Kinetics of Lead Halide Perovskite Quantum Dots. *Science* **2022**, *377* (6613), 1406−1412.
(52) Akkerman, Q. A. Spheroidal Cesium Lead Chloride−Bromide Quantum Dots and a Fast Determination of Their Size and Halide Content. *Nano Lett.* **2022**, *22* (20), 8168−8173.
(53) de Roo, J.; Ibáñez, M.; Geiregat, P.; Nedelcu, G.; Walravens, W.; Maes, J.; Martins, J. C.; van Driessche, I.; Kovalenko, M. v.; Hens, Z. Highly Dynamic Ligand Binding and Light Absorption Coefficient of Cesium Lead Bromide Perovskite Nanocrystals. *ACS Nano* **2016**, *10* (2), 2071−2081.
(54) Qu, L.; Peng, Z. A.; Peng, X. Alternative Routes toward High Quality CdSe Nanocrystals. *Nano Lett.* **2001**, *1* (6), 333−337.
(55) Carbone, L.; Nobile, C.; de Giorgi, M.; della Sala, F.; Morello, G.; Pompa, P.; Hytch, M.; Snoeck, E.; Fiore, A.; Franchini, I. R.; Nadasan, M.; Silvestre, A. F.; Chiodo, L.; Kudera, S.; Cingolani, R.; Krahne, R.; Manna, L. Synthesis and Micrometer-Scale Assembly of Colloidal CdSe/CdS Nanorods Prepared by a Seeded Growth Approach. *Nano Lett.* **2007**, *7*, 2942−2950.

https://doi.org/10.1021/acs.nanolett.2c04532
Nano Lett. 2023, 23, 667−676

(56) Abécassis, B.; Testard, F.; Spalla, O.; Barboux, P. Probing in Situ the Nucleation and Growth of Gold Nanoparticles by Small-Angle X-Ray Scattering. *Nano Lett.* **2007**, *7* (6), 1723−1727.
(57) Abécassis, B.; Bouet, C.; Garnero, C.; Constantin, D.; Lequeux, N.; Ithurria, S.; Dubertret, B.; Pauw, B. R.; Pontoni, D. Real-Time in Situ Probing of High-Temperature Quantum Dots Solution Synthesis. *Nano Lett.* **2015**, *15* (4), 2620−2626.
(58) Castro, N.; Bouet, C.; Ithurria, S.; Lequeux, N.; Constantin, D.; Levitz, P.; Pontoni, D.; Abécassis, B. Insights into the Formation Mechanism of CdSe Nanoplatelets Using in Situ X-Ray Scattering. *Nano Lett.* **2019**, *19* (9), 6466−6474.
(59) Wu, L.; Willis, J. J.; McKay, I. S.; Diroll, B. T.; Qin, J.; Cargnello, M.; Tassone, C. J. High-Temperature Crystallization of Nanocrystals into Three-Dimensional Superlattices. *Nature* **2017**, *548* (7666), 197−201.
(60) Wu, L.; Fournier, A. P.; Willis, J. J.; Cargnello, M.; Tassone, C. J. In Situ X-Ray Scattering Guides the Synthesis of Uniform PtSn Nanocrystals. *Nano Lett.* **2018**, *18* (6), 4053−4057.
(61) Seibt, S.; Zhang, H.; Mudie, S.; Förster, S.; Mulvaney, P. Growth of Gold Nanorods: A SAXS Study. *J. Phys. Chem. C* **2021**, *125* (36), 19947−19960.
(62) Burian, M.; Amenitsch, H. Dummy-Atom Modelling of Stacked and Helical Nanostructures from Solution Scattering Data. *IUCrJ.* **2018**, *5* (4), 390−401.
(63) Yoon, S. J.; Stamplecoskie, K. G.; Kamat, P. v. How Lead Halide Complex Chemistry Dictates the Composition of Mixed Halide Perovskites. *J. Phys. Chem. Lett.* **2016**, *7* (7), 1368−1373.
(64) Hui, J.; Jiang, Y.; Gökçinar, Ö. Ö.; Tang, J.; Yu, Q.; Zhang, M.; Yu, K. Unveiling the Two-Step Formation Pathway of Cs_4PbBr_6 Nanocrystals. *Chem. Mater.* **2020**, *32* (11), 4574−4583.
(65) Boles, M. a.; Engel, M.; Talapin, D. v. Self-Assembly of Colloidal Nanocrystals: From Intricate Structures to Functional Materials. *Chem. Rev.* **2016**, *116*, 11220−11289.
(66) Huang, H.; Feil, M. W.; Fuchs, S.; Debnath, T.; Richter, A. F.; Tong, Y.; Wu, L.; Wang, Y.; Döblinger, M.; Nickel, B. Growth of Perovskite $CsPbBr_3$ Nanocrystals and Their Formed Superstructures Revealed by In Situ Spectroscopy. *Chem. Mater.* **2020**, *32* (20), 8877−8884.
(67) Abécassis, B.; Tessier, M. D.; Davidson, P.; Dubertret, B. Self-Assembly of CdSe Nanoplatelets into Giant Micrometer-Scale Needles Emitting Polarized Light. *Nano Lett.* **2014**, *14*, 710−715.
(68) Bodnarchuk, M. I.; Li, L.; Fok, A.; Nachtergaele, S.; Ismagilov, R. F.; Talapin, D. V. Three-Dimensional Nanocrystal Superlattices Grown in Nanoliter Microfluidic Plugs. *J. Am. Chem. Soc.* **2011**, *133* (23), 8956−8960.
(69) Montanarella, F.; Geuchies, J. J.; Dasgupta, T.; Prins, P. T.; van Overbeek, C.; Dattani, R.; Baesjou, P.; Dijkstra, M.; Petukhov, A. V.; van Blaaderen, A.; Vanmaekelbergh, D. Crystallization of Nanocrystals in Spherical Confinement Probed by in Situ X-Ray Scattering. *Nano Lett.* **2018**, *18* (6), 3675−3681.
(70) Nakagawa, F.; Saruyama, M.; Takahata, R.; Sato, R.; Matsumoto, K.; Teranishi, T. *In Situ* Control of Crystallinity of 3D Colloidal Crystals by Tuning the Growth Kinetics of Nanoparticle Building Blocks. *J. Am. Chem. Soc.* **2022**, *144* (13), 5871−5877.
(71) Mau, S.-C.; Huse, D. A. Stacking Entropy of Hard-Sphere Crystals. *Phys. Rev. E* **1999**, *59* (4), 4396−4401.
(72) Bolhuis, P. G.; Frenkel, D.; Mau, S.-C.; Huse, D. A. Entropy Difference between Crystal Phases. *Nature* **1997**, *388* (6639), 235−236.

https://doi.org/10.1021/acs.nanolett.2c04532
Nano Lett. 2023, 23, 667−676